# Decoupled Dynamic Control for Pitch and Roll Axes of the Unicycle Robot

Jaeoh Lee, Seongik Han, and Jangmyung Lee

***Abstract*—This paper proposes a decoupled control algorithm for a single-wheel (unicycle) balanced robot. A unicycle robot is controlled by two independent control laws: the method involving mobile inverted pendulum control for the pitch axis and the method involving reaction-wheel pendulum control for the roll axis. We assume that both roll dynamics and pitch dynamics are decoupled from each other. As a result, the roll and pitch dynamics are obtained independently and all interactions between them are considered disturbances. Each control law is implemented by an individual controller, i.e., fuzzy-sliding mode control for roll and linear quadratic regulator control for pitch. Fuzzy logic is utilized to compensate for the interactions between the pitch and roll dynamics in real time. The unicycle robot has two dc motors: one to drive the disk for roll and the other to drive the wheel for pitch. Since there is no force to change the yaw direction, the dynamics of the yaw direction is not changed in this paper. Algorithms for the decoupled dynamics were implemented in a real unicycle robot, which was made to follow a desired trajectory along a straight line. Angle data was obtained by fusion of the gyro sensor and accelerometer. The results of experiments conducted confirmed the effectiveness of our proposed control system.**

***Index Terms*—Decoupled dynamics, fuzzy logic, fuzzy-sliding mode control, linear quadratic regulator (LQR) control, unicycle robot.**

## I. Introduction

RESEARCH ON the single-wheel (unicycle) robot has been ongoing since the 1980s in the U.S., Europe, and Japan. A. Schoonwinkel of Stanford University proposed a linear dynamic model of the robot and presented its optimal motion control in his Ph.D. thesis in 1987 [1]. Prof. Yamafujii of Tokyo University also proposed a dynamic model of the robot as an upper turntable and a lower rotating wheel. He also implemented PI motion control for it in 1997 [2]. In 2005, M.-Q. Dao and K.-Z. Liu of Chiba University maintained the roll balance using two gyroscopes and an actuator, and the pitch balance using a rotating wheel. The rotational torque in the direction yaw was canceled out in opposite rotations. They obtained the dynamics based upon the Lagrangian of the system and implemented the gain-scheduling algorithm for robustness [3]. The roll axis control of the unicycle robot has recently been altered and studied by using two flying pans at both sides of the robot, where the PD and PID controllers have been adopted [4]. However, while there has been a lot of research focusing on the roll axis control of the robot, no research results have been reported for its velocity tracking control.

Over the last four years, several unicycle robots have been implemented in the Intelligent Robot Laboratory at Pusan National University. However, a dynamic model of the robot has proven too complex to be implemented in real time [5]–[7]. Intelligent algorithms that did not incorporate dynamic information also proved unsuccessful in the control of the trajectory of the robot. To overcome these difficulties, in this approach, the dynamics of the unicycle robot has been decoupled into two parts: roll axis and pitch axis dynamics. The coupling effects between the two axes are not considered in the dynamic models [8], [9]. However, in the roll control, the coupling effects are compensated by using a fuzzy sliding mode algorithm. The pitch axis is modeled as an inverted pendulum, while the roll axis is modeled as a reaction-wheel pendulum. The dynamics that were not modeled, such as disturbances, frictions, some coupling terms, and system uncertainties, were compensated for by using an equivalent control input to the sliding mode controller, which was obtained from fuzzy control logic. To minimize the chattering phenomenon of the sliding mode controller, the fuzzy-tuning scheme was adopted in the signum function, which is used as a switching function.

Because the pitch axis is modeled as an inverted pendulum, it is relatively robust against disturbances. As a result, a linear controller based upon the linear quadratic regulator (LQR) scheme was adopted in this research [10].

The unicycle robot consists of two dc motors: one for controlling the pitch axis and the other for controlling the roll axis. The motor's angle is measured by an encoder attached to the motor axis, and the robot angles (pitch, roll, and yaw) are measured by using a two-axis gyroscope and three-axis accelerometer. The decoupling control of the robot, gyroscopes, and accelerometers were utilized to measure the angle information of the robot.

In this paper, we discuss posture and motion controls of the unicycle robot. The paper consists of five sections including this introduction. In Section II, we discuss how the dynamics of the robot was derived based upon the Lagrangian method [11]. Section III introduces the design of the controllers, and Section IV illustrates the experimental environments. Section V demonstrates the experimental results for the posture and

Manuscript received September 21, 2011; revised March 8, 2012; accepted June 25, 2012. Date of publication July 12, 2012; date of current version May 2, 2013. This research was supported by The Ministry of Knowledge Economy (MKE), Korea, under the Human Resources Development Program for Specialized Navigation/Localization Technology Research Center support program supervised by the National IT Industry Promotion Agency (NIPA) (NIPA-2011-C7000-1001-0004). Corresponding author: J. Lee (e-mail: jmlee@pusan.ac.kr).

The authors are with the Department of Electronics Engineering, Pusan National University, Busan 609-735, Korea (e-mail: jaeoh2@pusan.ac.kr; snikhan@gmail.com; jmlee@pusan.ac.kr).

Color versions of one or more of the figures in this paper are available online at http://ieeexplore.ieee.org.

Digital Object Identifier 10.1109/TIE.2012.2208431

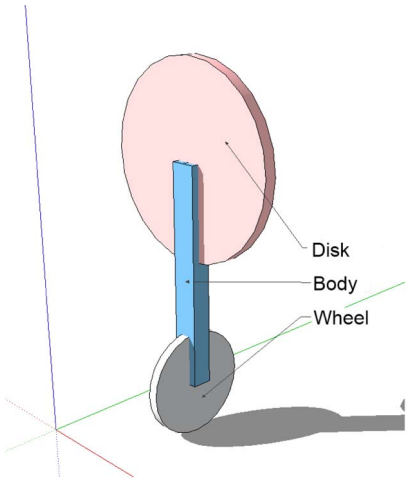


Fig. 1. Simplified model of the unicycle robot.

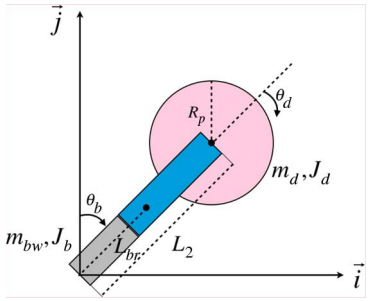


Fig. 2. Model of the unicycle robot for roll axis.

motion control of the unicycle robot and discusses some problems that remain. Section VI concludes this research and proposes future research work.

## II. Dynamic Modeling

In this section, we discuss how the dynamic models of the unicycle robot for the roll and pitch axes were derived using the Lagrangian method. Fig. 1 shows the unicycle robot developed in this research. It consists of a rotating disk, a robot body, and a rotating wheel. The mass of the rotating disk, the robot body, and the rotating wheel are represented as $m_d$, $m_b$, and $m_w$, respectively. The real experimental system is introduced in Section IV.

### A. Dynamic Model for Roll Axis

The roll dynamics are derived by viewing the unicycle robot as a reaction-wheel pendulum in which the rotation wheel and the robot body are assumed to be a single body [8], [9].

Fig. 2 shows the robot coordinates used to derive the roll dynamics. $L_2$ and $L_{br}$ represent the distances from the floor to the center of the rotation disk and to the center of mass of the rotation wheel-robot body compound object, respectively. $R_p$ and $\theta_d$ represent the radius and the angular displacement of the rotation disk, respectively. $\theta_b$ represents the roll angle of the robot.

To derive dynamic equations, the mass of the compound object is represented as $m_{bw}$, where $m_b$ and $m_w$ are the mass of the robot body and the wheel, respectively. Two position vectors, $\vec{r}_1$ and $\vec{r}_2$, are defined to derive the Lagrangian for the robot, where $\vec{r}_1$ and $\vec{r}_2$ are the vectors to the center of the rotation disk and to the center of the compound object, respectively

$$\begin{aligned}\vec{r}_1 &= L_{br}\sin\theta_b\vec{i} + L_{br}\cos\theta_b\vec{j}\\ \vec{r}_2 &= L_2\sin\theta_b\vec{i} + L_2\cos\theta_b\vec{j}.\end{aligned} \tag{1}$$

The kinetic energy of the robot, $T$, can be represented as

$$\begin{aligned}T = \frac{1}{2}m_{bw}(\vec{v}_1\cdot\vec{v}_1) + \frac{1}{2}m_d(\vec{v}_2\cdot\vec{v}_2)\\ +\frac{1}{2}J_b\dot{\theta}_b^2 + \frac{1}{2}J_d(\dot{\theta}_b+\dot{\theta}_d)^2\cos\theta_b\vec{j}\end{aligned} \tag{2}$$

where $\vec{v}_i = d\vec{r}_i/dt$, $J_d$ and $J_b$ are the rotational inertia of the rotation plate and the rotational inertia of the robot body-rotation wheel compound object, respectively.

The potential energy, $V$, can be represented as

$$V = m_{bw}gL_{br}\cos\theta_b + m_dgL_2\cos\theta_b \tag{3}$$

where $g = 9.8$ m/sec$^2$.

Therefore, the Lagrangian, $L$, can be represented as

$$\begin{aligned}L &= T - V\\ &= \frac{1}{2}m_{bw}(\vec{v}_1\cdot\vec{v}_1) + \frac{1}{2}m_d(\vec{v}_2\cdot\vec{v}_2)\\ &\quad + \frac{1}{2}J_b\dot{\theta}_b^2 + \frac{1}{2}J_d(\dot{\theta}_b+\dot{\theta}_d)^2\cos\theta_b\vec{j}\\ &\quad - m_{bw}gL_{br}\cos\theta_b - m_dgL_2\cos\theta_b.\end{aligned} \tag{4}$$

Using the Lagrange equation, we get

$$\frac{d}{dt}\frac{\partial L}{\partial\dot{\mathbf{q}}} - \frac{\partial L}{\partial\mathbf{q}} = \tau_q \tag{5}$$

where $\mathbf{q} = [\theta_b\ \theta_d]^T$ and $\tau_q = [\tau_b\ \tau_d]^T$.

The roll dynamics can be represented as

$$\left(J_b + L_{br}^2m_{bw} + L_2^2m_d\right)\ddot{\theta}_b - g(L_{br}m_{bw} + L_2m_d)\sin\theta_b = \tau_b \tag{6a}$$

$$J_d(\ddot{\theta}_d + \ddot{\theta}_b) = \tau_d \tag{6b}$$

where $\tau_d$ is the torque generated by the rotational disk motor and the torque applied to the pendulum, $\tau_b$, has the same magnitude in the opposite direction, that is, $\tau_b = -\tau_d$.

### B. Dynamic Model for Pitch Axis

The dynamic model for the pitch axis was derived as an inverted pendulum in which the rotational disk and the robot body were viewed as a single object [10]. Fig. 3 illustrates the robot coordinates used to derive the pitch dynamics. $l$ represents the distance from the center of the wheel to the mass center of the compound object consisting of the rotation disk and the robot body. $R_w$ is the radius of the rotation wheel, while $\theta$ and

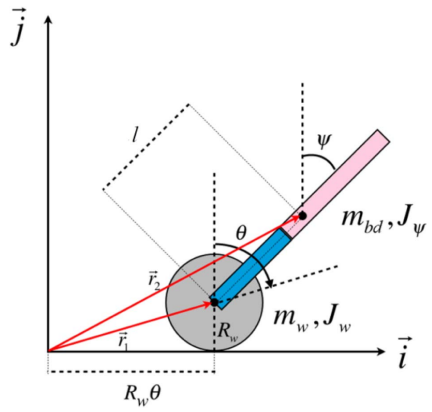


Fig. 3. Model of the unicycle robot for pitch axis.

$\psi$ represent the rotational angle of the wheel and the pitch axis angle, respectively.

For the pitch axis dynamics, the mass of the rotation wheel and the compounded mass of the robot body-rotational disk compound object are defined as $m_w$ and $m_{bd}$, respectively.

The positioning vectors, $\vec{r}_1$ and $\vec{r}_2$ are defined from the origin to the center of the rotational wheel and to the center of mass, $m_{bp}$, respectively, as follows:

$$\vec{r}_1 = R_w\theta\vec{i} + R_w\vec{j} \tag{7a}$$
$$\vec{r}_2 = (R_w\theta + l\sin\psi)\vec{i} + (R_w + l\cos\psi)\vec{j}. \tag{7b}$$

The kinetic energy of the robot, $T$, is represented as

$$T = \frac{1}{2}m_w(\vec{v}_1\cdot\vec{v}_1) + \frac{1}{2}m_{bd}(\vec{v}_2\cdot\vec{v}_2) + \frac{1}{2}J_w\dot{\theta}^2 + \frac{1}{2}J_\psi\dot{\psi}^2 + \frac{1}{2}n^2J_m(\dot{\theta}-\dot{\psi})^2 \tag{8}$$

where $\vec{v}_i = d\vec{r}_i/dt$, $J_w$, $J_\psi$, and $J_m$ are the inertias of the rotation wheel, the robot body-rotational disk compound object, and the motor armature, respectively, and n is the gear ratio.

The potential energy, $V$, can be represented as

$$V = m_wgR_w + m_{bd}g(R_w + l\cos\psi). \tag{9}$$

Therefore, the Lagrangian, $L$, can be obtained as

$$\begin{aligned} L &= T - V \\ &= \frac{1}{2}m_w(\vec{v}_1\cdot\vec{v}_1) + \frac{1}{2}m_{bd}(\vec{v}_2\cdot\vec{v}_2) + \frac{1}{2}J_w\dot{\theta}^2 + \frac{1}{2}J_\psi\dot{\psi}^2 \\ &\quad + \frac{1}{2}n^2J_m(\dot{\theta}-\dot{\psi})^2 - m_wgR_w - m_{bd}g(R_w + l\cos\psi). \end{aligned} \tag{10}$$

Using Lagrangian (5), the dynamic equations can be derived as

$$J_1\ddot{\theta} + J_3\ddot{\psi} + lm_{bd}R_w\sin\psi\dot{\psi}^2 = \tau_\theta \tag{11a}$$
$$J_2\ddot{\theta} + J_4\ddot{\psi} - glm_{bd}\sin\psi = \tau_\psi \tag{11b}$$

where $J_1 = J_w + J_mn^2 + (m_w + m_{bd})R_w^2$, $J_2 = lm_{bd}R_w\cos\psi - J_mn^2$, $J_3 = lm_{bd}R_w\cos\psi - J_mn^2$, and $J_4 = J_\psi + l^2m_{bd} + J_mn^2$. $\tau_\theta$ is the torque generated by the motor at the rotational wheel. Note that the $\tau_\psi$, the torque applied to the pendulum, is the opposite of the motor torque, that is, $\tau_\psi = -\tau_\theta$.

### C. Linear Dynamic Model of the Unicycle Robot

Using the upright conditions, $\sin\psi \approx \psi$ and $\dot{\psi}^2 = 0$, (11) can be represented as a linear system

$$\left[J_w + J_mn^2 + (m_w + m_{bd})R_w^2\right]\ddot{\theta} + \left[lm_{bd}R_w - J_mn^2\right]\ddot{\psi} = \tau_\theta \tag{12a}$$

$$\left[lm_{bd}R_w - J_mn^2\right]\ddot{\theta} + \left[J_\psi + l^2m_{bd} + J_mn^2\right]\ddot{\psi} - glm_{bd}\psi = \tau_\psi. \tag{12b}$$

To consider the motor dynamics with the robot dynamics [10], the dc motor torque T is represented as

$$T = n\frac{K_t}{R_m}\left(v + K_b(\dot{\psi} - \dot{\theta})\right) + f_m(\dot{\psi} - \dot{\theta}) \tag{13}$$

where $v$ is the applied voltage to the motor and $\dot{\psi} - \dot{\theta}$ represents the angular velocity of the wheel against the robot body. In addition, $K_t$ is the motor torque constant; $R_m$, the motor resistance; $f_m$, the motor friction coefficient; and $K_b$, the back e.m.f. constant. For simplicity, the motor inductance is neglected.

Using (13), the external torque required for the motor was obtained as

$$\tau_\theta = -\alpha v - \beta(\dot{\psi} - \dot{\theta}) \tag{14}$$
$$\tau_\psi = \alpha v + \beta(\dot{\psi} - \dot{\theta}) \tag{15}$$

where $\alpha = nK_t/R_m$ and $\beta = \alpha + f_m$.

Substituting (12a) and (12b) into (14) and (15),

$$\left(J_w + J_mn^2 + (m_w + m_{bd})R_w^2\right)\ddot{\theta} + (lm_{bd}R_w - J_mn^2)\ddot{\psi} + \beta\dot{\theta} - \beta\dot{\psi} = \alpha v \tag{16a}$$

$$(lm_{bd}R_w - J_mn^2)\ddot{\theta} + (J_\psi + l^2m_{bd} + J_mn^2)\ddot{\psi} - \beta\dot{\theta} + \beta\dot{\psi} - glm_{bd}\psi = -\alpha v. \tag{16b}$$

Setting the control input, $u$, as

$$u = v. \tag{17}$$

The (16a) and (16b) can be combined into a matrix equation as

$$E\begin{bmatrix}\ddot{\theta}\\ \ddot{\psi}\end{bmatrix} + F\begin{bmatrix}\dot{\theta}\\ \dot{\psi}\end{bmatrix} + G\begin{bmatrix}\theta\\ \psi\end{bmatrix} = Hu \tag{18}$$

where

$$E = \begin{bmatrix}\left(J_w + J_mn^2 + (m_w + m_{bd})R_w^2\right) & lm_{bd}R_w - J_mn^2\\ lm_{bd}R_w - J_mn^2 & J_\psi + l^2m_{bd} + J_mn^2\end{bmatrix}$$

$$F = \begin{bmatrix}\beta & -\beta\\ -\beta & \beta\end{bmatrix},\quad G = \begin{bmatrix}0 & 0\\ 0 & -glm_{bd}\end{bmatrix},\quad \text{and}\quad H = \begin{bmatrix}\alpha\\ -\alpha\end{bmatrix}.$$

Equation (18) is transformed into the state equation

$$\begin{bmatrix}\dot{\theta}\\ \dot{\psi}\\ \ddot{\theta}\\ \ddot{\psi}\end{bmatrix} = \begin{bmatrix}0 & 0 & 1 & 0\\ 0 & 0 & 0 & 1\\ 0 & A(3,2) & A(3,3) & A(3,4)\\ 0 & A(4,2) & A(4,3) & A(4,4)\end{bmatrix}\begin{bmatrix}\theta\\ \psi\\ \dot{\theta}\\ \dot{\psi}\end{bmatrix} + \begin{bmatrix}0\\ 0\\ B(3)\\ B(4)\end{bmatrix}u \tag{19}$$

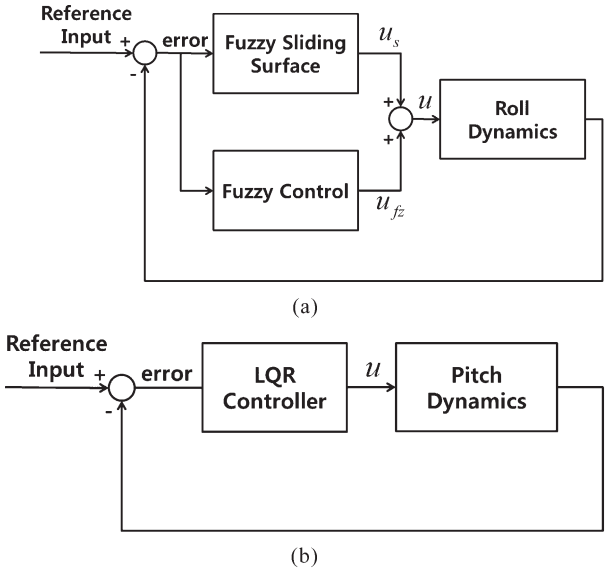


Fig. 4. (a) Control block diagram of the roll axis controller. (b) Control block diagram of the controller for the pitch axis.

where

$$\begin{aligned}
A(3,2) &= -glm_{bd}E(1,2)/\det(E)\\
A(4,2) &= glm_{bd}E(1,1)/\det(E)\\
A(3,3) &= -\left[\beta E(2,2)+\beta E(1,2)\right]/\det(E),\\
A(4,3) &= \left[\beta E(2,1)+\beta E(1,1)\right]/\det(E)\\
A(3,4) &= \left[\beta E(2,2)+\beta E(1,2)\right]/\det(E)\\
A(4,4) &= -\left[\beta E(2,1)+\beta E(1,1)/\det(E)\right.\\
B(3) &= \alpha\left[E(2,2)+E(1,2)\right]/\det(E)\\
B(4) &= -a\left[E(2,1)+E(1,1)\right]/\det(E).
\end{aligned}$$

Note that $\det(E)$ represents the determinant of matrix E and $E(i,j)$ represents the ith row and jth column element of matrix E.

## III. Design of the Decoupled Controller

In this section, we discuss the controllers for the roll and pitch axes were designed based upon the decoupled dynamics derived in Section II. Two independent controllers were concurrently applied for the control of the robot. For the roll axis, the fuzzy-sliding mode controller was used, and for the pitch axis control, the LQR control scheme was utilized.

As shown in Fig. 4(a), the fuzzy algorithms have been applied for the gain tuning of the sliding mode controller and for obtaining the equivalent input, $u_{eq}$. The out of the fuzzy sliding surface, $u_s$, is added to the input for keeping the system states on the sliding surface.

Fig. 4(b) represents the control block diagram for the pitch axis, in which the LQR controller was implemented, resulting in a linearized system.

### A. Design of the Sliding Mode Controller for the Roll Axis

To design the sliding mode controller, the sliding surface was set as follows:

$$s(t) = k_1 e(t) + \dot{e}(t) \tag{20}$$

where $k_1$ is the gain constant to be determined. $e(t)$, the difference between the real roll angle, $\theta_b$, and the reference angle, $\theta_{\rm ref}$, is given as

$$e(t) = \theta_b(t) - \theta_{\rm ref}(t). \tag{21}$$

To obtain an equivalent input, $u_{eq}$, the $\dot{s}$ term can be obtained from (20) as

$$\begin{aligned}
\dot{s} &= k_1\dot{e} + \ddot{e}\\
&= k_1\dot{e} - \ddot{\theta}_{\rm ref} + \ddot{\theta}_b\\
&= k_1\dot{e} - \ddot{\theta}_{\rm ref} + \frac{1}{D_r}\left(g(L_{br}m_{bw} + L_2 m_d)\sin\theta_b - \tau_r\right)
\end{aligned} \tag{22}$$

where $\ddot{\theta}_b$ can be obtained from (6) and $D_r = J_b + L_{br}^2 m_{bw} + L_2^2 m_d$.

The control input, $u_{eq}$, can be selected to satisfy the condition $\dot{s} = 0$ such that the control state variables of $e(t)$ and $\dot{e}(t)$ gradually approach to zero [12]

$$u_{eq} = k_1\dot{e} - \ddot{\theta}_{\rm ref} + \frac{1}{D_r}g(L_{br}m_{bw} + L_2 m_d)\sin\theta_b. \tag{23}$$

To keep the system states on the sliding surface, the control input $u$ can be set as

$$u = u_{eq} + \gamma_1 \cdot \mathrm{sgn}(s) \tag{24}$$

where $\gamma_1 \cdot \mathrm{sgn}(s)$ denotes the $u_s$, $\gamma_1 > 0$ and $\mathrm{sgn}(s)$ is defined as follows:

$$\mathrm{sgn}(s) = \begin{cases} -1 & \text{if } s < 0\\ 1 & \text{if } s > 0. \end{cases} \tag{25}$$

To prove the stability of the control system, the Lyapunov function candidate $V$ is defined as

$$V = \frac{1}{2}s^2. \tag{26}$$

For the stability condition, $\dot{V} = s\dot{s} \le 0$, (20) and (22) are substituted into s and $\dot{s}$. When the $u_{eq}$ is substituted for u in (24), $\dot{V}$ is derived as follows:

$$\begin{aligned}
\dot{V} &= s\dot{s}\\
&= s\left(k_1\dot{e} - \ddot{\theta}_{\rm ref} + \frac{1}{Den_r}g(L_{br}m_{bw} + L_2 m_d)\sin\theta_b - u\right)\\
&= -\gamma_1|s| \le 0.
\end{aligned} \tag{27}$$

By selecting $u$ using (24), $\dot{V} = s\dot{s} \le 0$ condition has been satisfied such that the system states exist on the sliding surface [13].

### B. Design of LQR Controller for Pitch Axis

Using the linear dynamics of the pitch axis, an LQR controller was designed. The weighting matrices Q and R were selected as follows:

$$\mathbf{Q} = \begin{bmatrix} 10 & 0 & 0 & 0\\ 0 & 100 & 0 & 0\\ 0 & 0 & 1 & 0\\ 0 & 0 & 0 & 10 \end{bmatrix} \tag{28a}$$

$$\mathbf{R} = 1. \tag{28b}$$

Using the real parameters shown in Table III, the optimal gain was obtained by using the LQR toolbox in MATLAB [14], [15] as $K = [-3.16\ \ -103.2\ \ -3.39\ \ -7.32]$. During

TABLE I
TWO INPUT/ONE OUTPUT FUZZY RULE FOR $\delta$

| $\delta$ | | Change of error | | | | | | | | | | |
|---|---|---|---|---|---|---|---|---|---|---|---|---|
| | | NH | NL | NB | NM | NS | Z | PS | PM | PB | PL | PH |
| E | NH | PH | PH | PH | PH | PH | PH | PL | PB | PM | PS | Z |
| R | NL | PH | PH | PH | PH | PH | PL | PB | PM | PS | Z | NS |
| R | NB | PH | PH | PH | PH | PL | PB | PM | PS | Z | NS | NM |
| O | NM | PH | PH | PH | PL | PB | PM | PS | Z | NS | NM | NB |
| R | NS | PH | PH | PL | PB | PM | PS | Z | NS | NM | NB | NL |
| | Z | PH | PL | PB | PM | PS | Z | NS | NM | NB | NL | NH |
| | PS | PL | PB | PM | PS | Z | NS | NM | NB | NL | NH | NH |
| | PM | PB | PM | PS | Z | NS | NM | NB | NL | NH | NH | NH |
| | PB | PM | PS | Z | NS | NM | NB | NL | NH | NH | NH | NH |
| | PL | PS | Z | NS | NM | NB | NL | NH | NH | NH | NH | NH |
| | PH | Z | NS | NM | NB | NL | NH | NH | NH | NH | NH | NH |

the experiments, the velocity gain K [4] was adjusted in order to reduce the vibration of robot body.

Using the K, the control input is given as

$$u = -\mathbf{KX} \tag{29}$$

where $\mathbf{X} = [e_\theta \ e_\psi \ \dot{\theta} \ \dot{\psi}]^T$, $e_\theta = \theta - \theta_{\rm ref}$ and $e_\psi = \psi - \psi_{\rm ref}$. Note that $\psi_{\rm ref}$ is the reference angle of the pitch axis.

### C. Design of Fuzzy Sliding Mode Controller

To obtain the equivalent control input, $u_{eq}$, in the sliding mode algorithm, fuzzy logic was utilized in this research [16]–[19]. Even though the $u_{eq}$ has already been determined in (23) for the sliding mode control of the roll axis, the decoupled roll dynamics itself does not include the coupling terms, frictions, disturbance, and uncertainties in the system. This limits the accuracy of the equivalent control input for the optimal control. Fuzzy logic resolves these time-varying and nonlinear effects in real time in determining $u_{eq}$.

The fuzzy rules are represented as

$$\text{Rule } i : \textbf{IF} \text{ error is } F_e^i \ \textbf{AND} \text{ change-of-error is } F_c^i$$
$$\textbf{THEN} \text{ ouput is } \delta_i$$

where $\delta_i$, $i = 1, 2, \ldots, m$ are singleton values, $F_e^i$ and $F_c^i$ are fuzzy sets for the error and the derivative of the error, respectively.

The triangular membership functions are used for both the IF and THEN parts. The fuzzy rules are summarized in Table I.

In Table I and Fig. 5, N and P imply negative and positive, respectively, while H, L, B, M, S, and Z represent huge, large, big, medium, small, and zero, respectively.

For the defuzzification, the center of gravity method was used as

$$u_{fz} = \frac{\sum_{i=1}^{m} w_i \cdot \delta_i}{\sum_{i=1}^{m} w_i} \tag{30}$$

where $w_i$ is the weight for the ith rule.

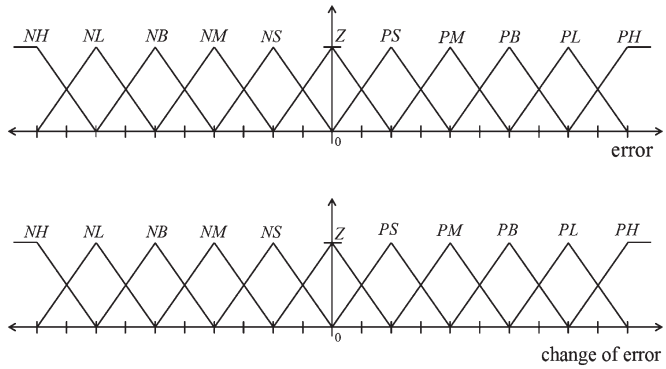


Fig. 5. Membership functions of fuzzy rules.

TABLE II
FUZZY RULES FOR $\gamma$ FUZZY-TUNING

| s | NH | NL | NB | NM | NS | Z | PS | PM | PB | PL | PH |
|---|---|---|---|---|---|---|---|---|---|---|---|
| $\gamma$ | H | L | B | M | S | Z | S | M | B | L | H |

To determine the stability of this fuzzy-sliding mode algorithm, the roll dynamics in (6a) can be defined as

$$\ddot{\theta}_b = f_{\rm roll}(q) - u \tag{31}$$

where $f_{\rm roll}(q)$ includes the uncertain time varying and nonlinear terms in the roll dynamics. From (24), for the control input $u$, $u_{eq}$ is replaced by $u_{fz}$ and the result is substituted into (27) for $\dot{V} = s\dot{s}$

$$\begin{aligned}\dot{V} &= s\dot{s} \\ &= s\left(k_1\dot{e} - \ddot{\theta}_{\rm ref} + f_{\rm roll}(q) - u\right) \\ &= s\left(k_1\dot{e} - \ddot{\theta}_{\rm ref} + f_{\rm roll}(q) - u_{fz} - \gamma_1 {\rm sgn}(s)\right)\end{aligned} \tag{32}$$

where the condition $u_{fz} \le k_1\dot{e} - \ddot{\theta}_{\rm ref} + f_{\rm roll}(q)$ is satisfied by the fuzzy rules, which guarantee the stability condition for $\dot{V} = s\dot{s} \le 0$.

### D. Reduction of Chattering Phenomenon

Chattering phenomenon occurs in the sliding mode control due to the signum switching function. When $\gamma$ is decreased, in an attempt to reduce the chattering, the settling time of the state variables become longer. To counter this phenomenon, in this study, a fuzzy-tuning algorithm was developed to eliminate the time delay while reducing the chattering. $\gamma$ is reduced near the sliding surface to reduce the boundary layer, and it is kept high at the initial stage to shorten the settling time [20].

The fuzzy rules for this are as follows:

$$\text{Rule i} : \textbf{IF } s \text{ is } F_s^i \ \textbf{THEN} \text{ ouput is } \gamma_i$$

where s represents the sliding surface, $\gamma_i$, $i = 1, 2, \ldots, m$ is a singleton value, and $F_s^i$ is the fuzzy set for s. The fuzzy rules are summarized in Table II.

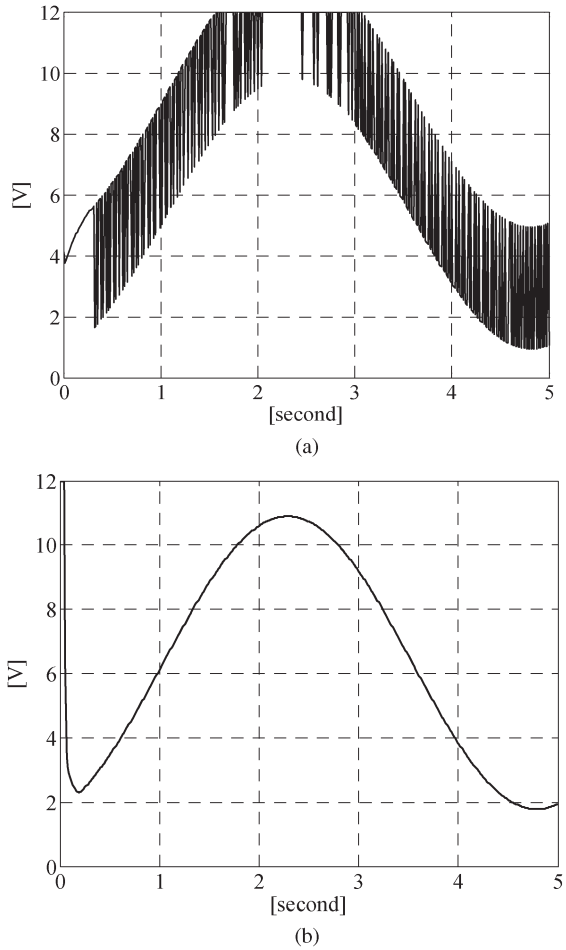


Fig. 6. (a) Chattering in the control input. (b) Simulation of fuzzy-tuning to reduce chattering.

In Table II, N and P represent negative and positive, respectively, while H, L, B, M, S, and Z represent huge, large, big, medium, small, and zero, respectively.

The center of gravity method is used for the defuzzification. Note that $\gamma$ is kept as a positive constant to satisfy the following condition: $\dot{V} = s\dot{s} \leq 0$.

Fig. 6(a) shows the chattering in the control input before application of the fuzzy rules.

As shown in Fig. 6(b), the chattering phenomenon disappears from the control input when fuzzy rules are applied to tune gains in real time.

## IV. Experimental Environments

Fig. 7 shows a photograph of the actual unicycle robot used in this research. The gyroscope and accelerometers are located at the center of the robot body, the main controller is placed on the upper body, and the motor drives are located on the lower body. The NTARS of NTREX Corporation with ARM Cortex-M3 (LM3S8962) processor were used for the angle sensor. MAXON Corporation dc motors were used and the angular data obtained by encoders. For the motor drives, NT-DC20A H-bridge types were used. The cables in Fig. 7 provided the power to the robot. The timing belt for the pitch drive is connected to the dc motor from the lower wheel. This is designed not to cause unstable structure of the roll axis when the pitch driving motor is directly connected to the lower wheel. However, the roll driving motor is directly connected to the disk. The initial design of the timing belt for the roll driving was changed to the direct drive since the backlash causes the roll balance control to be difficult. The antenna on top of the robot connects the Bluetooth module to the computer to send the robot states to the computer. It also receives commands from the computer. To get the higher inertia, the disk is designed to have a circular frame and balanced weight.

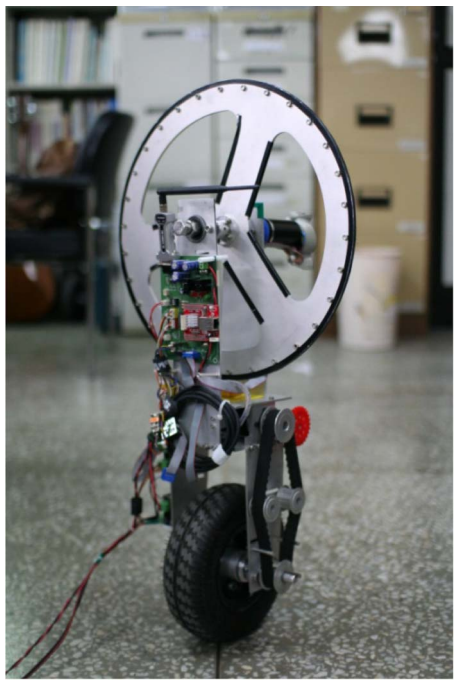

Fig. 7. Photograph of the actual unicycle robot.

Dynamic parameters of the robot are summarized in Table III. The inertia of the robot, $J_d$, $J_b$, $J_\psi$, and $J_w$ have been estimated by the robot structure and the motor parameters are provided by the manufactures.

For the three inputs of ramp, ladder, and parabolic shapes, the robot's angles, velocities, and positions were measured to evaluate the performance of the proposed decoupled control scheme.

## V. Experimental Results and Discussions

### A. Ramp Input

To check the position/velocity tracking capability of the unicycle robot, a ramp input was applied to the robot for a distance of 3.3 m. During the motion, the angle, velocity, and distance data were collected and compared to the desired values, as shown in Figs. 8 and 9.

In Fig. 8, the reference input, the current travel distance of the unicycle robot, and the error between the two values are represented by the dotted line, solid line, and the broken lines, respectively. Fig. 9 shows the current and reference velocities as dotted and solid lines, respectively.

TABLE III
PARAMETERS OF THE UNICYCLE ROBOT

| Symbol | Parameter | Value |
|---|---|---|
| $m_d$ | Mass of rotational disk | 1.225 $Kg$ |
| $m_b$ | Mass of robot body | 3.664 $Kg$ |
| $m_w$ | Mass of rotational wheel | 1.300 $Kg$ |
| $m_{bd}$ | $m_b + m_d$ | 4.889 $Kg$ |
| $m_{bw}$ | $m_b + m_w$ | 4.964 $Kg$ |
| $R_w$ | Radius of rotational wheel | 0.110 $m$ |
| $R_p$ | Radius of rotational disk | 0.200 $m$ |
| $L_2$ | Distance to the center of the rotational disk from the origin | 0.570 $m$ |
| $L_{br}$ | $L_{br} = L_2/2$ | 0.285 $m$ |
| $l$ | Distance to the center of $m_{bp}$ from the center of rotational wheel | 0.330 $m$ |
| $J_d$ | Inertia of rotational disk | 0.0402 $m$ |
| $J_b$ | Inertia of the robot body and the rotational wheel | 0.5295 $Kg\,m^2$ |
| $J_\psi$ | Inertia of the robot body and the rotational disk | 0.7208 $Kg\,m^2$ |
| $J_w$ | Inertia of rotational wheel | 0.0079 $Kg\,m^2$ |
| $J_m$ | Inertia of motor armature | 0.0001 $Kg\,m^2$ |

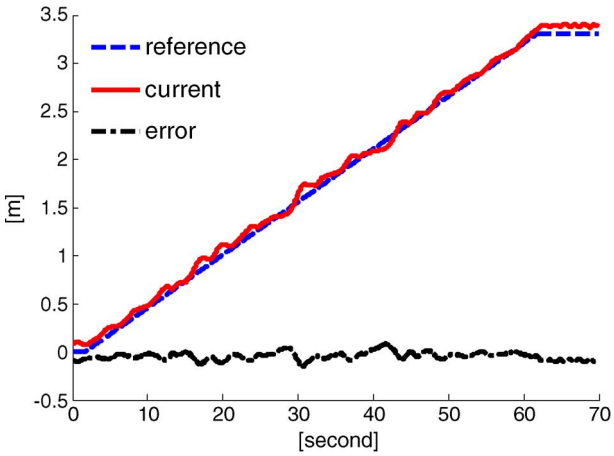


Fig. 8. Tracking performance of the rotational wheel.

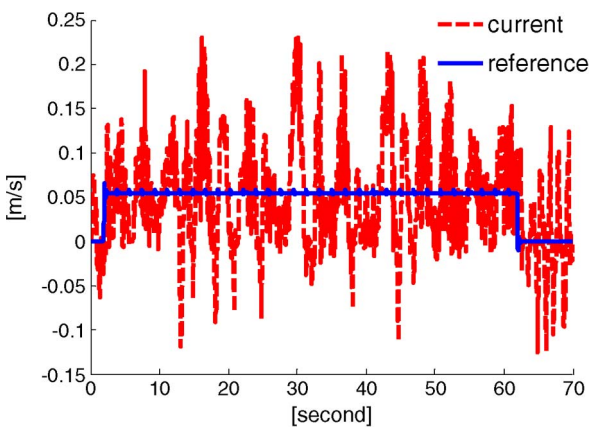


Fig. 9. Velocity tracking of the rotational wheel.

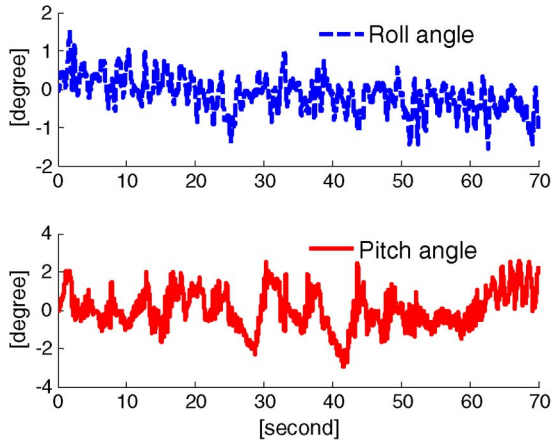


Fig. 10. Roll and pitch angle errors of the single wheel robot.

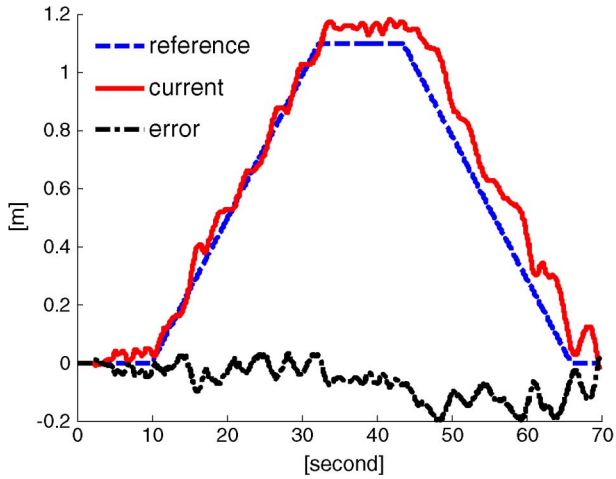


Fig. 11. Tracking performance of the rotational wheel.

Fig. 10 shows the roll and pitch angle errors of the robot, represented by the dotted and solid lines, respectively.

Data collected from the robot during its 3.3-m travel showed that the roll and pitch angle errors were kept within approximately $\pm 1^\circ$ and $\pm 2^\circ$, respectively. In other words, the unicycle robot motion is stabilized and has good tracking performance within the motion range.

### B. Ladder Input

To check the forward and backward tracking capability of the robot, a ladder input was applied to the robot to move it 1.1 m forward and then back to the original position. During the forward and backward motion, the angle, velocity, and position data were recorded and plotted as shown in Figs. 11 and 12.

In Fig. 11, the reference input, current travel distance of the robot, and the error between the two values are represented by the dotted line, solid line, and the broken lines, respectively.

Fig. 12 represents the current and reference velocities using dotted and solid lines, respectively.

As shown in Fig. 13, the roll and pitch angle errors were kept within about $\pm 2^\circ$ and $\pm 4^\circ$, respectively. Note that the angle errors increased greatly because of the velocity change in the middle of the trajectory. However, the robot motion was

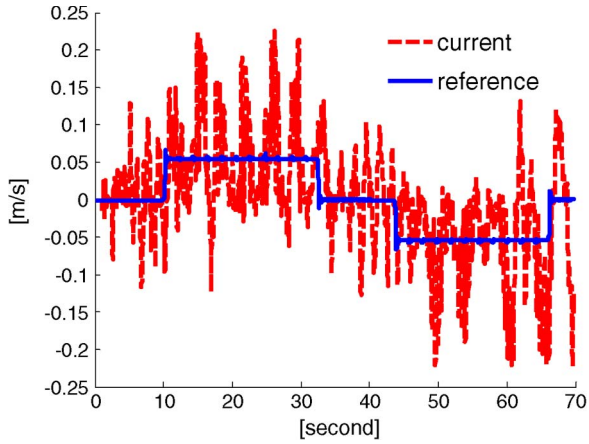


Fig. 12. Velocity tracking of the rotational wheel.

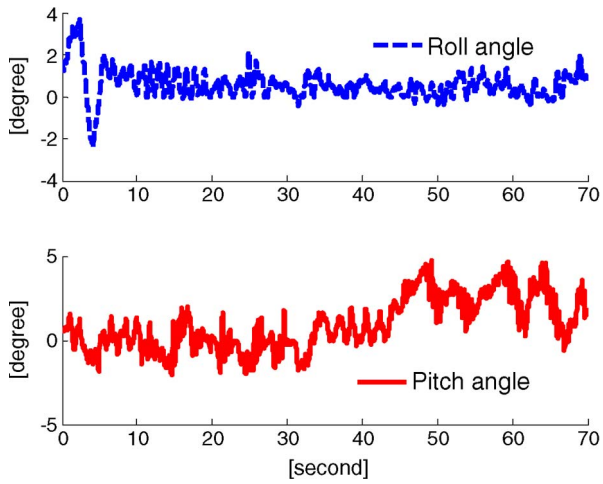


Fig. 13. Roll and pitch angle errors of the unicycle robot.

also stabilized and had good tracking performance within the round trip.

### C. Parabolic Input

To check the position/velocity tracking capability of the robot, a parabolic input was applied to the robot up to 2.8 m. During the motion, the angle, velocity, and distance data were collected and compared with the desired values in Figs. 14 and 15.

In Fig. 14, the reference input, the current travel distance of the robot, and the error between the two values are represented by the dotted line, solid line, and the broken lines, respectively.

Fig. 15 shows the current and reference velocities by the dotted and solid lines, respectively.

As shown in Fig. 16, the roll and pitch angle errors were kept within approximately $\pm 1^\circ$ and $\pm 2^\circ$, respectively. Note that even though the pitch error increased to over $4^\circ$ at 30 s, it was soon stabilized. This may have happened due to the irregularity of the surface.

The performance of the unicycle robot was evaluated on the basis of the three different trajectory-following tasks. In all cases, the robot maintained a stable posture while following the desired position/velocity trajectory. An intrinsic problem

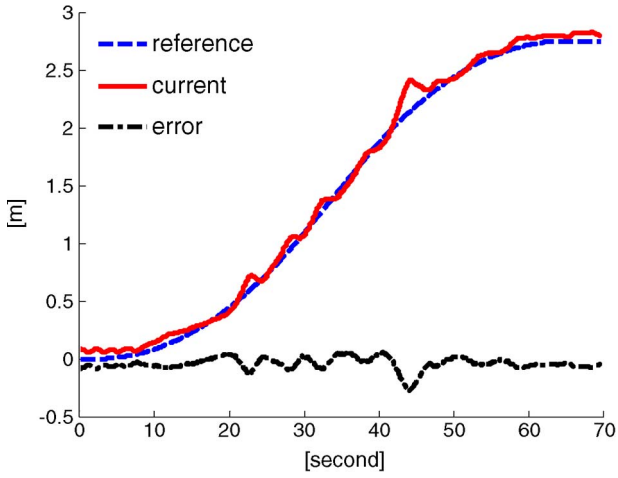


Fig. 14. Tracking performance of the rotational wheel.

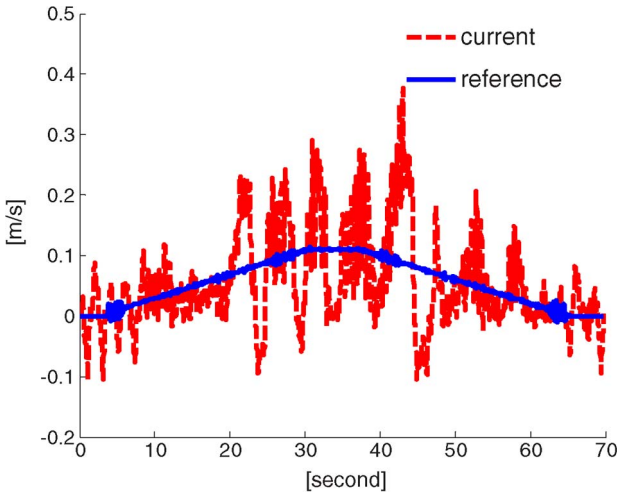


Fig. 15. Velocity tracking of the rotational wheel.

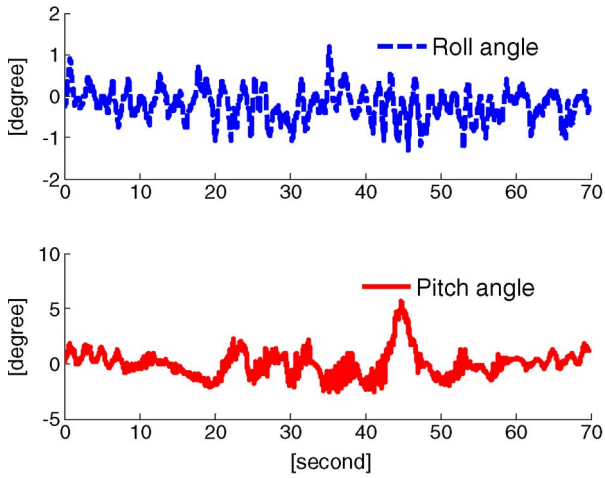


Fig. 16. Roll and pitch angle errors of the unicycle robot.

suffered by the robot was the high velocity error sustained while following the trajectory. This stemmed from the fact that balancing the robot was given a higher priority than dynamically following the desired trajectory. When the velocity control gain was increased in the experimental system, the velocity error was

reduced. However, this caused the robot to become unstable and fall to the floor.

## VI. Conclusion

In this paper, we proposed a decoupled control algorithm for posture and motion control of a single wheel balanced (unicycle) robot. The robot dynamics were derived for each of the roll and pitch axes separately as they were decoupled from each other. The coupling effects for the roll axis were compensated for using stable posture control by a fuzzy sliding mode controller. Fuzzy rules were used to obtain an equivalent control input for the sliding mode controller in order to maintain the stability of the robot under the existence of unmodeled dynamics such as coupling terms, unknown friction terms, disturbances, and system uncertainties. The fuzzy rules were also utilized to tune the signum function gains in the sliding mode controller, in order to reduce the phenomenon of chattering. The dynamics of the robot were derived on the basis of the Lagrangian method. The LQR scheme was also adopted for the control of the pitch axis. The velocity control widens the applications of the unicycle robot. For an example, the unicycle robot can move to a desired position at a desired time, which enables to avoid the obstacles in the traveling path. The velocity of the unicycle robot remains lower than 0.1 m/s due to the speed limit of the gyroscope and accelerometers. In a future study, we plan to solve this problem by using fast and stable sensors.

## References


[1] A. Schoonwinkel, "Design and test of a computer stabilized unicycle," Ph.D. dissertation, Stanford Univ., Stanford, CA, 1987.

[2] Z. Sheng and K. Yamafuji, "Postural stability of a human riding a unicycle and its emulation by a robot," *IEEE Trans. Robot. Autom.*, vol. 13, no. 5, pp. 709–720, Oct. 1997.

[3] M.-Q. Dao and K.-Z. Liu, "Gain-scheduled stabilization control of a unicycle robot," *JSME Int. J.*, vol. 48, no. 4, pp. 649–656, Jan. 2005.

[4] J.-H. Lee, H.-J. Shin, S.-J. Lee, and S. Jung, "Novel air blowing control for balancing a unicycle robot," in *Proc. IEEE/RSJ Int. Conf. Intell. Robots Syst.*, 2010, pp. 2529–2530.

[5] S. Kim, J. Lee, J. Hwang, B. Ahn, and J. Lee, "Dynamic modeling and performance improvement of a unicycle robot," *J. Inst. Contr. Robot. Syst.*, vol. 16, no. 11, pp. 1074–1081, 2010.

[6] H. Lim, J.-M. Hwang, B.-H. Ahn, and J.-M. Lee, "Robust yaw motion control of unicycle robot," *J. Inst. Contr. Robot. Syst.*, vol. 15, no. 11, pp. 1130–1136, 2009.

[7] H. Jin, J. Hwang, and J. Lee, "A balancing control strategy for a one-wheel pendulum robot based on dynamic model decomposition: Simulations and experiments," *IEEE/ASME Trans. Mechatronics*, vol. 16, no. 4, pp. 763–768, Aug. 2011.

[8] D. Buccieri, D. Perritaz, P. Mullhaupt, Z. Jiang, and D. Bonvin, "Velocity-scheduling control for a unicycle mobile robot: Theory and experiments," *IEEE Trans. Robot.*, vol. 25, no. 2, pp. 451–458, Apr. 2009.

[9] K. N. Srinias and L. Behera, "Swing-up strategies for a reaction wheel pendulum," *Int. J. Syst. Sci.*, vol. 39, no. 12, pp. 1165–1177, Dec. 2008.

[10] NXTway-GS (self-balancing two-wheeled robot) controller design, LEGO Mindstorm, Enfield, CT, Tech. Rep. [Online]. Available: http://www.mathworks.com/matlabcentral/fileexchange/19147

[11] K. Erbatur, M. O. Kaynak, and A. Sabanovic, "Modeling with Euler-Lagrange equation and cybernetical analysis for a unicycle robot," in *Proc. 2nd Int. Conf. Intell. Comput. Technol. Autom.*, 2009, pp. 108–111.

[12] R. S. Munoz-Aguilar, A. Doria-Cerezo, E. Fossas, and R. Cardoner, "Sliding mode control of a stand-alone wound rotor synchronous generator," *IEEE Trans. Ind. Electron.*, vol. 58, no. 10, pp. 4888–4897, Oct. 2011.

[13] Z. Zhu, Y. Xia, and M. Fu, "Adaptive sliding mode control for attitude stabilization with actuator saturation," *IEEE Trans. Ind. Electron.*, vol. 58, no. 10, pp. 4898–4907, Oct. 2011.

[14] R. C. Dorf and R. H. Bishop, *Modern Control System, 10th Edition: Optimal Control System*. Upper Saddle River, NJ: Pearson, 2005.

[15] Y. Tanaka and T. Murakami, "A study on straight-line tracking and posture control in electric bicycle," *IEEE Trans. Ind. Electron.*, vol. 56, no. 1, pp. 159–168, Jan. 2009.

[16] Y.-H. Chang, C.-W. Chang, J.-S. Taur, and C.-W. Tao, "Fuzzy swing-up and fuzzy sliding-mode balance control for a planetary-gear-type inverted pendulum," *IEEE Trans. Ind. Electron.*, vol. 56, no. 9, pp. 3751–3761, Sep. 2009.

[17] A. Hazzab, I. K. Bousserhane, M. Kamli, and M. Rahli, "Adaptive fuzzy sliding mode controller for induction motor control," in *Proc. ICTTA*, 2006, pp. 163–168.

[18] R.-J. Wai, C.-M. Lin, and C.-F. Hsu, "Adaptive fuzzy sliding-mode control for electrical servo drive," *Fuzzy Sets Syst.*, vol. 143, no. 2, pp. 295–310, Apr. 2004.

[19] D.-S. Kim, D.-W. Kim, G.-T. Park, and S.-J. Seo, "Control of hydraulic excavator using self tuning fuzzy sliding mode control," *J. Contr. Autom. Syst. Eng.*, vol. 11, no. 2, pp. 160–166, 2005.

[20] Y.-S. Huang, C.-C. Sung, and C.-S. Yu, "Reduced order fuzzy sliding mode control for linear synchronous motor systems," in *Proc. ICIT*, Mar. 2010, pp. 392–397.


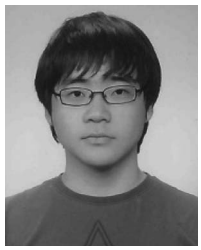

**Jaeoh Lee** received the B.S. degree in electrical engineering from Pusan National University, Busan, Korea, in 2010. Currently, he is working toward the M.S. degree in electrical engineering from Busan National University, Busan.

His current research interests include modern control techniques, robot-balancing problems, modeling, and nonlinearcontrol.

**Seongik Han** received the B.S. and M.S. degrees in mechanical engineering and the Ph.D. degree in mechanical design engineering from Pusan National University, Busan, Korea, in 1987, 1989, and 1995, respectively.

From 1995 to 2009, he was an Assistant Professor of Electrical Automation at Suncheon First College, Korea. Presently, he is a Research Professor in the Department of Electrical Engineering, Pusan National University. His research interests include intelligent control, nonlinear control, robotic control, and active noise and vibration control.

**Jangmyung Lee** received the B.S. and M.S. degrees in electronic engineering from Seoul National University, Seoul, Korea, in 1980 and 1982, respectively, and the Ph.D. degree in computer engineering from the University of Southern California, Los Angeles, in 1990.

Since 1992, he has been a Professor with the Intelligent Robot Laboratory, Pusan National University, Busan, Korea. His current research interests include intelligent robotic systems, ubiquitous ports, and intelligent sensors.

Dr. Lee is the past President of the Korean Robotics Society. He is the Head of National Robotics Research Center, SPENALO.